Towards a Glomerulus Nanoscale Spatial Atlas

Adilijiang Ali

A thesis

Submitted in partial fulfillment of the

requirements for the degree of

Master of Science

University of Washington

2022

Committee:

Joshua Vaughan

Ashleigh Theberge

Program Authorized to Offer Degree:

Chemistry

University of Washington

Abstract

Towards a Glomerulus Nanoscale Spatial Atlas

Adilijiang Ali

Chair of the Supervisory Committee:
Joshua Vaughan
Department of Chemistry

The glomerulus is the basic filtration apparatus of the kidney, where thousands of the capillary-rich structures function to remove waste products from the blood stream while retaining macromolecules and blood cells. This thesis develops the groundwork for establishing a Glomerular Nanoscale Spatial Atlas (GNSA). The GNSA will be the first resource of its kind, which will include a detailed annotated collection of high spatial resolution (~50 nm) three-dimensional (3D) reconstructions of glomeruli obtained from healthy, aged, and diseased kidney tissues in mouse and human. Data from a single analyzed glomerulus of a healthy female mouse was used to develop this pipeline and is presented here. Fundamental glomerular structures such as the Bowman's capsule, Bowman's space, glomerular basement membrane, mesangium, and arterioles were segmented, reconstructed, and quantitatively analyzed. Four types of glomerular cells, parietal epithelial cells, glomerular endothelial cells, podocytes, and mesangial cells were manually identified based on the size, shape, and position of the cell nuclei within the glomerular space. Several quantitative

parameters relating to cell nuclei were explored with the goal of finding potential classifiers to fully automate cell identification for future 3D reconstructions. We hypothesize that establishing and refining the GNSA will aid in revealing the global linkages among glomerular structures and supply a more robust understanding of the glomerulus as a unity that could doubtless deliver novel facets of glomerular diseases that have not been explored.

TABLE OF CONTENTS

List of Figures

List of Tables

ACKNOWLEDGEMENTS

First of all, I would like to thank my advisor Prof. Joshua Vaughan for his meticulous support throughout my time at the Vaughan lab. This thesis could not be completed without the support from Prof. Vaughan. Before joining the group, I was perplexed and didn't know what I could do due to my lack of scientific research experience. He welcomed me into the group and provided me with tremendous amount of help starting from the first day. We had many inspiring and encouraging discussions on a weekly basis, which slowly equipped me well with the skills and knowledge for becoming a rigorous researcher. He provided me with a lot of opportunities for both developing my individual skills and working as a qualified team member. Had it not been for the professor's help, I would not have been admitted to the PhD degree in chemistry at UW. I would like to give a special thank our post-doc, Chetan Poudel, for helping me extensively throughout my thesis work here. He helped me to get started to get into my work, by both providing valuable scientific knowledge and technical skills, which had greatly impacted me in developing a scientific mindset. He was always so patience with me when I had questions and encountered problems. I would also like to appreciate the remaining members of the Vaughan group, Madeline Wong, Marcus Woodworth, Chenyi Mao (former member), Ziyu Guo, Chris Kim, Hannah Perry, for their support both in science and in life as good friends. Additionally, I would like to thank Dr. Nathaniel Peters and Dr. Wai Pang Chan for providing precious software and instruments I used for my thesis work.

I want to send my sincerest appreciation to my families, both the ones back in China and the furry ones that accompany me here in the states. It has been eight years since I came to the United States. My parents have never stopped giving me their utmost support during this time.

Even though we have not seen each other for nearly six years, they still love me and support every decision I make without reservation. They made me feel that they are always mentally by my side, even though we are physically thousands of miles away. Their encouragements supported me in living and struggling in this foreign country while pursuing my dream of becoming a scientist. Finally, I want to thank my furry family, my cats Ginger and Shadow, and my dog Yoyo. When I was in a bad mood, when I felt lost about my future, and when I missed my family, they were always there by my side and gave me emotional support, helping me get through the difficult day.nUnfortunately, Ginger left me last year because of an accident. Her passing has made me realize that accidents can happen at any moment, and you never know which will come first, accident or tomorrow. It taught me to cherish and enjoy every minute of every day of life. Although Ginger has left our family, I will never forget her help and love for me, and she will forever be in my heart.

Introduction:

Kidneys are essential organs that play a critical role that are involved in regulating blood pressure, maintaining the balance between water, salt, and minerals, and most importantly, filtration of waste products from the blood [1]. Impaired kidney functions can lead to various kidney diseases, both acute (sudden failure of the kidney function) and chronic (gradual loss of kidney function overtime), and eventually lead to kidney failure. Even in healthy aging, the number of functional unit of the kidney, the nephron, decreases substantially and leads to substantially diminished filtration capacity [2], and several studies have shown that the risk of kidney diseases is remarkably high with aging [2]–[6].

The kidney is a bean-like organ composed of two main layers, the outer layer cortex and the inner medulla layer called the renal pyramid. An artery bearing unfiltered blood flows into these layers through the renal pelvis (**Figure 1A**) and branches into capillaries, which enters the basic functional unit of the kidney, the nephron (**Figure 1B**). Each nephron consists of a renal corpuscle, a proximal convoluted tube (PCT), a loop of Henle, and a distal convoluted tubule (DCT). Blood filtration starts as the glomerulus of the renal corpsule passes water and small molecules to the PCT while retaining large molecules such as proteins and cells. As the filtered blood exits the renal corpuscle and enters the PCT, molecules with nutritional significance, such as glucose, amino acids, and small peptides, are reabsorbed into nearby capillaries. Additional reabsorption is continued in the loop of Henle, a U-shaped tubule that facilitates the recovery of water and sodium chloride from the urine. The DCT then connects and ascends back to the cortex region while reabsorbing small molecules like water and ions. Eventually, the collecting ducts gather the remaining filtrates from multiple nephrons and reabsorb more water, producing concentrated urine for excretion.

As the first step of the blood filtration system, the proper development and preservation of the glomeruli are crucial to the regular functioning of the kidney. A considerable number of kidney problems, such as focal segmental glomerulosclerosis and IgA nephropathy, are caused by the structural and functional changes of the glomeruli[7]–[11]. The glomerulus is a network of capillaries called the glomerular tuft enclosed by a pouch-like membranous structure called Bowman's capsule (**Figure 1C**). These capillaries consist of a thin fenestrated layer of glomerular endothelial cells (GECs) surrounded by three layers: the mesangium, the glomerular basement membrane (GBM), and podocytes. As the core stalk of the glomerulus, the mesangium is made up of mesangial cells (MCs) and the extracellular matrix created around them called the mesangial matrix [12], [13]. GBM, on the other hand, is the non-cellular layer outside of the fenestrated endothelium and the mesangium, similar to the mesangial matrix but different in composition [13]–[16]. Lastly, the podocytes line the exterior face of capillaries which cover the outer capillary surface with closely interdigitated extensions called foot processes. A unique cell-to-cell junction connects these interdigitated foot processes called the slit diaphragm (**Figure 1D**), which helps maintain a defined distance between foot processes and provides additional structural support to the capillary network [17]. The podocytes, along with the fenestrated endothelium and the GBM, collectively form the glomerular filtration barrier (GFB), a three-layered filtration barrier (**Figure 1D**) that acts as a size-selecting sieve in which water and small solutes are freely permeable while retaining larger-sized proteins, macromolecules, and cells in the blood [18], [19].

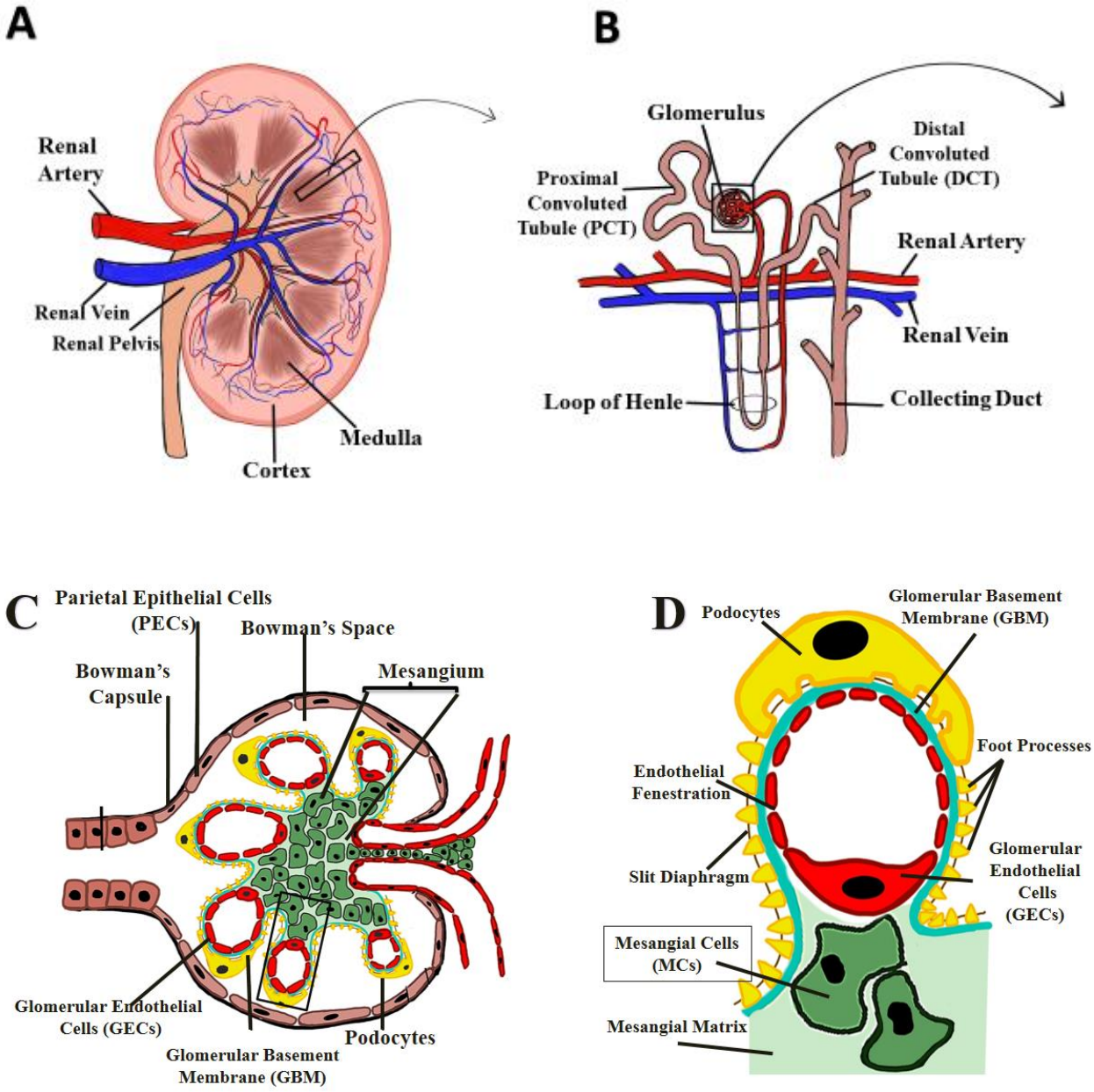

Figure 1. Basic anatomy of (A) Kidney; (B) Nephron; (C) Glomerulus; (D) Glomerular filtration barrier (GFB).

Glomerular morphology is altered in a variety of glomerular diseases, and nephrologists or renal pathologists carefully monitor glomerular morphology using light and electron microscopy

in order to better understand or diagnose and treat the specific disease [20]–[22]. Light microscopy (LM) is a powerful tool used in studies of the kidney [23]–[27] as it enables examination of overall physiology of the kidney the localization and identification of key molecules with high specificity. In many glomerular diseases, morphological changes can be easily seen using routine LM, but some glomerular diseases are more subtle and require examination at very high spatial resolution via EM. For example, minimal change disease (MCD) is among the most common causes of the nephrotic syndrome. It is characterized by the effacement of podocyte foot processes in glomeruli causing protein to leak through the GFB [28]–[30]. As the name MCD implies, these changes on foot processes are so subtle that they are only visible via EM and appear to be "normal' under LM. Electron microscopy (EM), on the other hand, provides nanoscale snapshots of glomerular ultrastructure with a significant enhancement of spatial resolution (1-10nm) as compared to LM. Therefore, EM has been widely used to detect subtle changes in fine structures of podocyte foot processes [21], [22], [27] and the GBM [27]. Aside from the resolution enhancement, EM is able to reveal general physiology of a sample with lower specificity as compared to the LM. Due to their complementary capabilities both EM and LM and are widely used for the study glomerular structures and the diagnosis of glomerular diseases.

These traditional methods are powerful but face several significant drawbacks. First, these measurements are primarily made on two-dimensional thin sections from glomeruli, which creates challenges with interpretation and might not capture key details evident in 3D data sets. Studying thin sections is not very helpful in exploring features that exhibit strong spatial characteristics such as glomerular capillary connectivity and continuity [20]. Second, knowledge of structures and morphology of glomeruli are built upon separate studies of individual substructures that come from the same kidney but different glomeruli. The direct correlation among these structures is therefore

complicated and can produce contradicting results. Third, the recent development of super-resolution optical microscopy techniques [31]–[34] (discussed further below) has enabled the study of the glomerulus at higher spatial resolution [23], [26], [35], [36]. However, such methods are often associated with elaborate and costly instruments and laborious acquisition and analysis procedures. The above limitations have generally shaped the field's approach to analyzing the glomeruli's limited portion or features.

Some 3D reconstruction and analysis work has previously been used to explore the spatial properties and characteristics of the various glomerular structures. Burghardt and coworkers reconstructed the three-dimensional structures of complete podocytes and their environments. They discovered that slit diagrams are not formed within foot processes of the same podocytes. Such information is never found in two-dimensional studies or partial reconstruction work on podocytes. In addition, they also found that podocyte foot processes exhibited more cell-to-cell contact interactions than slit diagrams, which is also missing information from partial analysis of podocytes [22]. In another study, the Terasaki group analyzed the blood space of whole mouse glomeruli using an advanced 3D serial sectioning EM pipeline and uncovered a clear separation between the afferent and efferent arteriole branches where it appears that blood could cross within this zone without being filtered [20]. Again, this information is found to be unreachable in two-dimensional and partial analysis of the glomerular capillary network. Studying only specific intact structures in 3D has already revealed structural information that has never been explored in 2D. The glomerulus is a complex structure, similar to a machine, and regular functioning of each individual component collectively contributes to the overall performance of the glomerulus. Previous work has extensively explored the local changes to structures in glomerular diseases. However, could these changes lead to global changes of the glomerulus? Or are these changes

accompanied by the changes that are distant from the well-characterized location? The underlining relationships and coordination among structures that more distant to each other, which are not easily detectable or utterly absent in two-dimensional or partial analysis of the glomerulus, are largely unexplored in the field. We hypothesize that by quantifying the glomerulus as a whole functioning unit could aid in exploring the global relationships among glomerular structures and provide a better understanding of the glomerulus as a unity, which could potentially deliver novel aspect of glomerular diseases that have never been explored.

To close these technical and knowledge gaps, this thesis aims to build the infrastructure for a Glomerular Nanoscale Spatial Atlas (GNSA) which will be the first resource in the field to provide high-resolution annotated data sets of whole mouse glomeruli for healthy, diseased, and aged tissue. The GNSA will provide detailed 3D models that annotate all major glomerulus structural components (Bowman's capsule, glomerular basement membrane, capillary lumen, and Bowman's space) and their statistical information not limited to surface areas, volumes, spatial orientation, and network analysis, as well as the locations of four primary glomerular cell types, the podocytes, mesangial cells (MCs), glomerular endothelial cells (GECs), and parietal epithelial cells (PECs). Furthermore, the statistical observables provided in the GNSA can be spatially directly related to one another within the same glomerulus, rather than correlations among data sets measured using different assays in different glomeruli. Furthermore, the models for glomeruli in different conditions (young, aged, diseased) may be compared with each other. The central goal of the GNSA is to identify previously unknown glomerular phenotypes at the whole-glomerulus level, and to create digital resources, both raw and annotated datasets, freely accessible online to the general public, including researchers, nephrologists, pathologists, and medical engineers for facilitating a better scientific understanding of glomerular diseases. One day, it will eventually

lead to more effective diagnosis and treatments of glomerular diseases.

In establishing the GNSA, the challenge is to provide feature-rich data in 3D for each glomerulus as a whole unit while maintaining a high spatial resolution. To overcome this, two major considerations have to be taken into account: the spatial resolution of imaging, and the generality of the staining method.

Resolution in fluorescence microscopy studies has been limited by the diffraction limit of the light [31]–[34]. Light, as a wave, when passing through an aperture, will diffract and create a radial pattern with intercalating bright and dark bands due to the constructive/destructive interactions between light waves. Light emitted from a point source (e.g., a fluorophore) on the sample passes through an objective and creates a similar 3-dimensional diffraction pattern called the point spread function (PSF) with a central high peak surrounded by a series of descending peaks surrounding it. The size of the PSF is determined by both the wavelength (λ) of the light source and the numerical aperture (NA) of the objective lens, which are be related to each other with equation: $d=0.61\lambda/\mathrm{NA}$ describing the closest distance between two point sources where the PSFs can be well separated from each other. Two objects can only be resolved if separated at a distance that is greater than half of the PSF's central peak width (FWHM). Theoretically, the larger the NA of an objective lens, the smaller the diffraction limit, better the resolution. However, in practice, the NA can only be so large (~1.4), limiting the resolution of typical light microscopy to around 250 nm laterally.

Multiple optical methods are available to solve the limitation imposed by the diffraction limit, including super-resolution methods such as super-resolution structured illumination microscopy (SR-SIM), stimulation emission depletion microscopy (STED) and stochastic optical reconstruction microscopy (STORM), all of which achieve improved resolution by reducing the

size of the PSF. However, as discussed earlier, these super-resolution methods often require highly specialized instruments. The more recent development of expansion microscopy (ExM) has allowed an alternative solution that uses the physical expansion of the specimen to overcome the problems introduced by the diffraction limit [37], [38]. In ExM, a specimen is uniformly expanded (e.g., fourfold) in all directions, with the result that features closer than the diffraction limit can be resolved after expansion because they are physically moved apart. This is achieved using simple chemicals and procedures accessible by most laboratories and compatible with familiar diffraction-limited microscopes [39], [40]. ExM works by first growing a swellable polymer network around the tissue, then degrading the mechanical support with proteases (ExM) [39] or high-temperature detergent homogenization (MAP) [41]. Finally, the sample is expanded by immersion in deionized water, achieving a physical magnification of the sample. We have chosen to use ExM as our primary imaging modality while establishing the GNSA due to the following reasons: 1) It provides a high resolution (up to 50 nm laterally) for resolving key glomerular structures; 2) Implementing 3D and multichannel imaging using ExM is relatively straightforward; 3) The requirements for skills and instrument are much less than demanding than other methods that provide comparable resolution. A potential downside is that expansion might not be uniform, however, careful validation can be done to help minimize this possibility.

Another consideration to be taken into account while building the GNSA is the labeling modality of the specimen. Routine LM of kidney tissue and glomeruli frequently uses hematoxylin & eosin stain (H&E) and related pathology stains [42], [43], or the direct labeling of specific molecules using immunostaining with antibodies [44], [45]. H&E stain is considered the “gold standard” in medical histology [43]. Hematoxylin by itself does not stain the tissue; it is normally used along with cationic metal, often aluminum, which forms a positively charged complex that

labels negatively charged DNA within the nucleus of cells a purplish blue color. Eosin is a negatively charged dye that stains the extracellular matrix and cytoplasm. Depending on the composition differences of the tissue, eosin can display different levels of pinkness. Though it provides generality by enabling visualization of various critical features of the glomerulus, its affinity-based nature has limited its compatibility with expansion microscopy. Many steps in ExM, including washing, gelation, and high-temperature denaturation, can easily result in loss of fluorescent eosin signal. Additionally, non-fluorescent histology stains (e.g., hematoxylin) are poorly suitable for volumetric imaging.

On the other hand, immunofluorescence has an excellent compatibility with ExM [26], [40]. It provides specific labeling of individual structures of the glomerulus with high specificity and the antibody stains can be tethered covalently to the hydrogel [39], [40], [46], [47]. However, specific stains are required for each structure. Due to the limited spectral channels, immunofluorescence can only reveal a limited number of features instead of the general physiology. One could surpass this with spectral unmixing techniques to achieve multiplexed imaging [48], [49], but it requires sufficient knowledge about computational analysis and complex mathematical algorisms. To overcome these considerations, I will use for the GNSA a general physiology stain recently developed by the Vaughan group called fluorescent labeling of abundant reactive entities (FLARE) [50], [51].

FLARE is a simple chemical staining method that combines the advantages of both affinity-based stains and immunofluorescence maintaining adequate retention of fluorescent labels while revealing key landmarks of the glomerulus simultaneously. It enables the labeling of three general types of biological macromolecules including carbohydrates, proteins, and nucleic acids/DNA (**Figure 2B**). FLARE works by first oxidizing carbohydrates on the specimen into

aldehydes and chemically linking them to commercially available hydrazide-functionalized fluorescence dyes; this procedure is similar to the classic periodic-acid Schiff (PAS) histology stain. Next, the primary amines commonly found in all proteins are labeled with reactive and commercially available NHS-functionalized dyes. Finally, the DNA is labeled using standard DNA-binding fluorescent dyes like Hoechst or SYBR Green. To preserve proteins structure within the sample, a protein-retaining variant of ExM called magnified analysis of proteome (MAP) is used [41], [50], [51].

By combining FLARE, MAP, and confocal microscopy techniques, the data sets acquired provide high-resolution images of whole individual glomeruli with relatively straightforward procedures and the no need of highly specialized instruments, labeled using general stains that reveal key structures. The workflow of creating the GNSA (**Figure 2A**) is composed of six parts: sample preparation, expansion and staining, imaging, segmentation, rendering, and then computational analysis of the results.

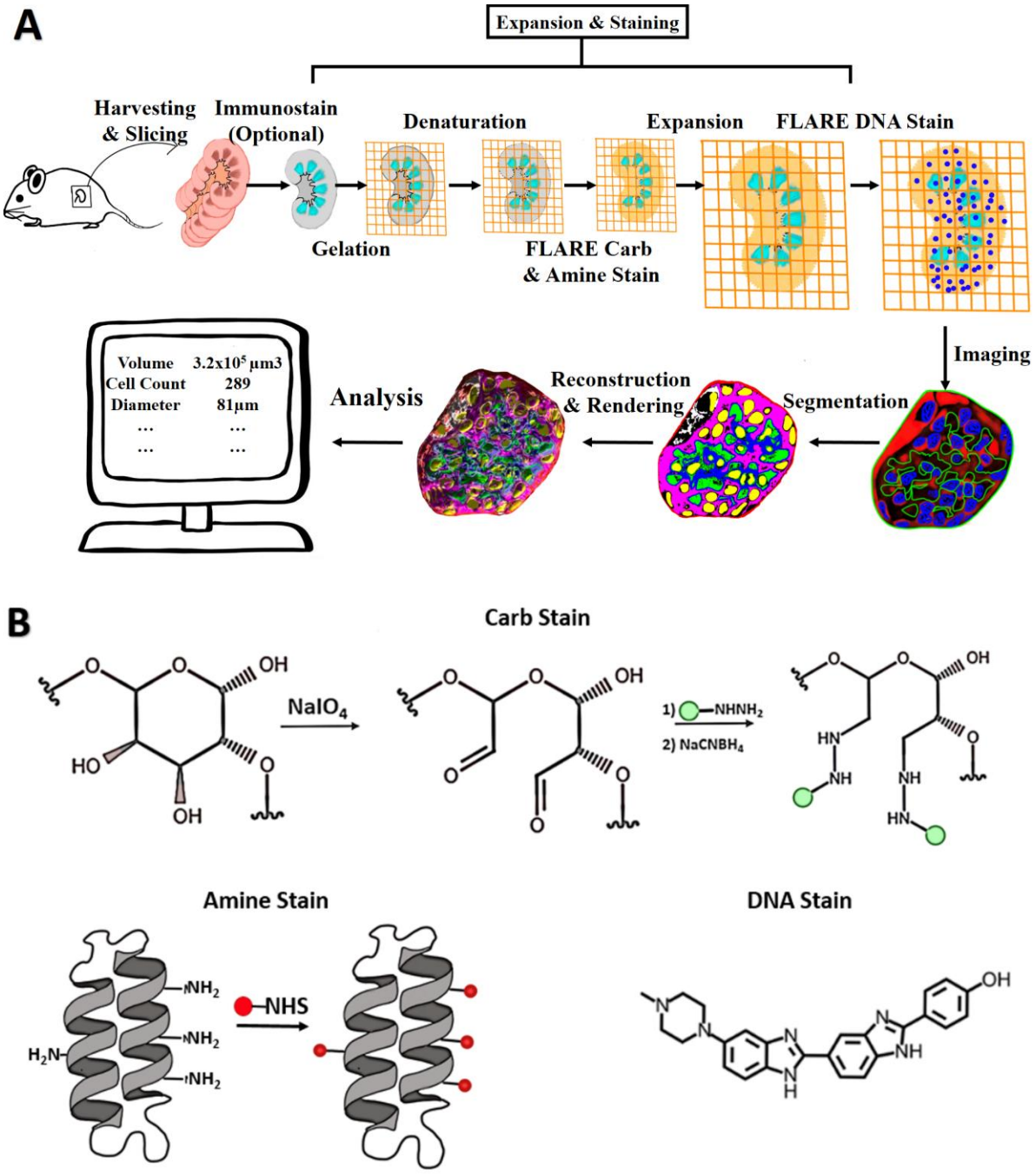

Figure 2. (A) Schematic illustration of the workflow for creating the GNSA. (B) FLARE Stain principles. Vicinal diols of carbohydrates are oxidized to aldehydes with sodium periodate, which is then reacted with hydrazide-functionalized fluorophores and stabilized by reducing with sodium cyanoborohydride. Primary amine groups on proteins are labeled by reacting with NHS-functionalized fluorophores. DNA is labeled using conventional DNA dye (Hoechst or SYBR Green).

Results:

Imaging a 3D z-stack of a whole intact glomerulus

Whole glomeruli within expanded and stained hydrogels were imaged on a Nikon [A1R HD25] point-scanning confocal microscope at an effective spatial resolution of roughly 100 nm in pre-expansion units (**Figure 3**). There are roughly 12,000 glomeruli within a mouse kidney [52], [53], however, only 3-5 whole, intact glomeruli were present per 100 µm kidney section due to both the working distance of the objective and positioning of the glomeruli within the tissue sections. The resulting image stack revealed key structural components of the glomerulus and structures surrounding it, using just the simple 3-channel FLARE stain. The carbohydrate stain (green) labeled membranous structures such as glomerular/PCT basement membrane, Bowman's capsule, and blood vessels, whereas the amine stain (red) labeled protein-rich structures such as mitochondria. Nuclei were labeled using the Hoechst stain.

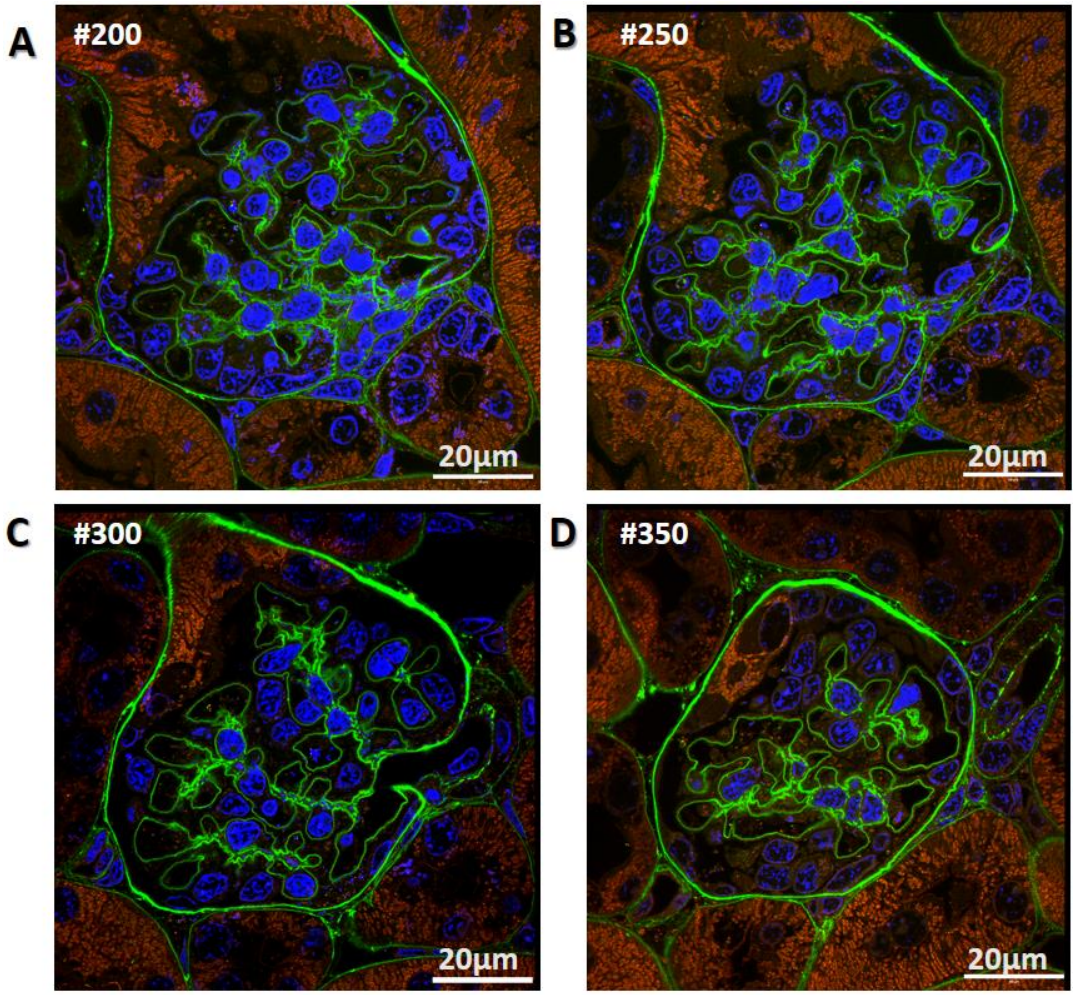

Figure 3. FLARE-stained expanded whole glomerulus imaged with a point-scanning confocal microscope, 40× water immersion lens. **(A)- (D)** show cross-sections #200, #250, #300 and #350 from a single image stack of 428 images. Green=carbohydrates; red=amine, blue=nuclei. Scale bars are shown in pre-expansion units.

Computational segmentation of key glomerular structures

We sought to identify the major structures and cell positions within the glomerulus. This was done through a combination of manual and semi-automated segmentation. First, the nuclei were segmented by tracing the periphery of each nucleus and filling the space within them. The Bowman's capsule and the GBM & mesangium were segmented by manually tracing the gray and

blue arrows indicated in the carbohydrate channel that are enriched at basement membranes (**Figure 4, carb channel**). We defined the glomerular blood space as the actual space where blood will flow freely within the capillaries. Therefore, the blood space was segmented by first filling the space enclosed by the segmented GBM & mesangium and then subtracting the amine signals and the segmented nuclei within this space. The blood space outside the glomerulus was segmented by first tracing out the afferent and efferent arterioles indicated by the red arrows (**Figure 4, carb channel**) and filling the space inside them. Lastly, the Bowman's space is the region of a glomerulus where the filtered blood will flow into and connects to the PCT. Hence, we defined the Bowman's space as the spaces between the Bowman's capsule and the GBM & mesangium where there is no signal for all three channels. It was then segmented by inverting the amine and carbohydrate channels and subtracting the blood space and the nuclei.

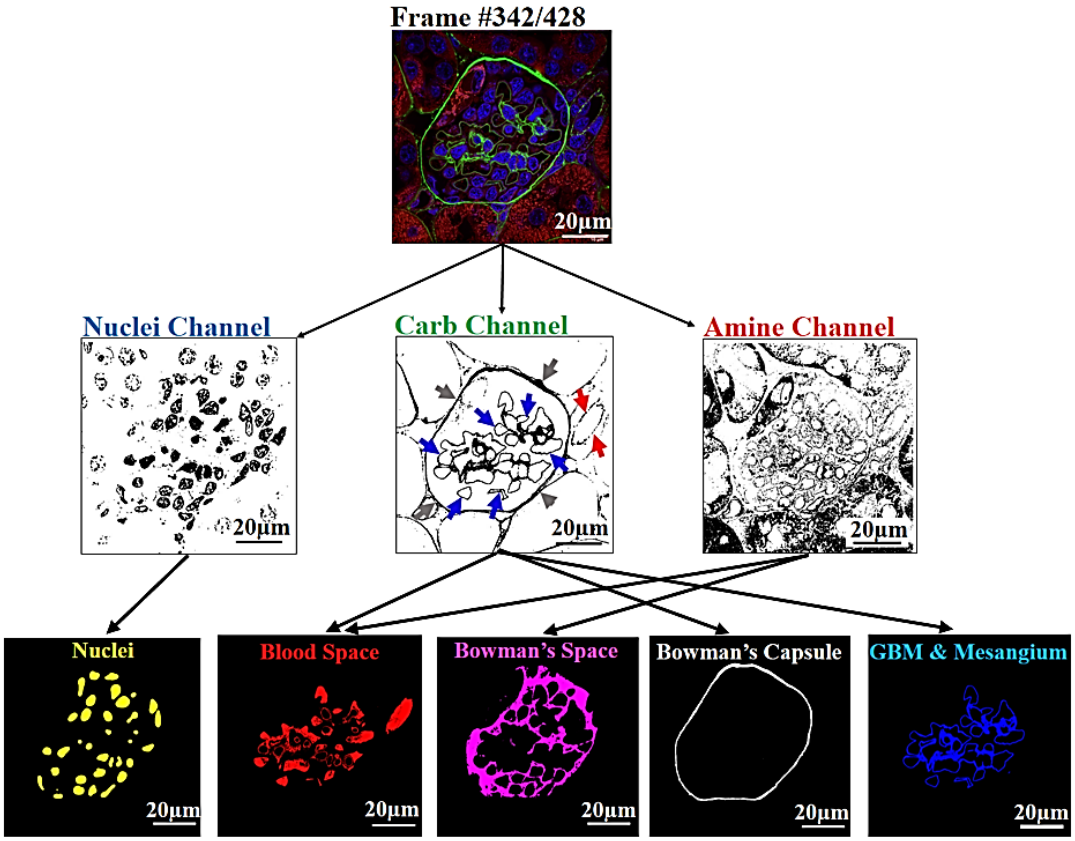

Figure 4. Schematic showing the process of segmenting five key glomerular structures from a single FLARE-stained image**.** Scale bars are shown in pre-expansion units.

3D reconstruction and rendering and statistics of key glomerular structures

To explore spatial relationships among the segmented structures with respect to the whole glomerulus, the five-channel segmented stack was then reconstructed and rendered in 3D using the surface creation tool on IMARIS image analysis software. As a result, five key structural components could be easily viewed as individual objects (**Figure 5A-E**) or as a composite (**Figure 5**F). The 3D rendering also allows the observation of the relative position and layering of different structures.

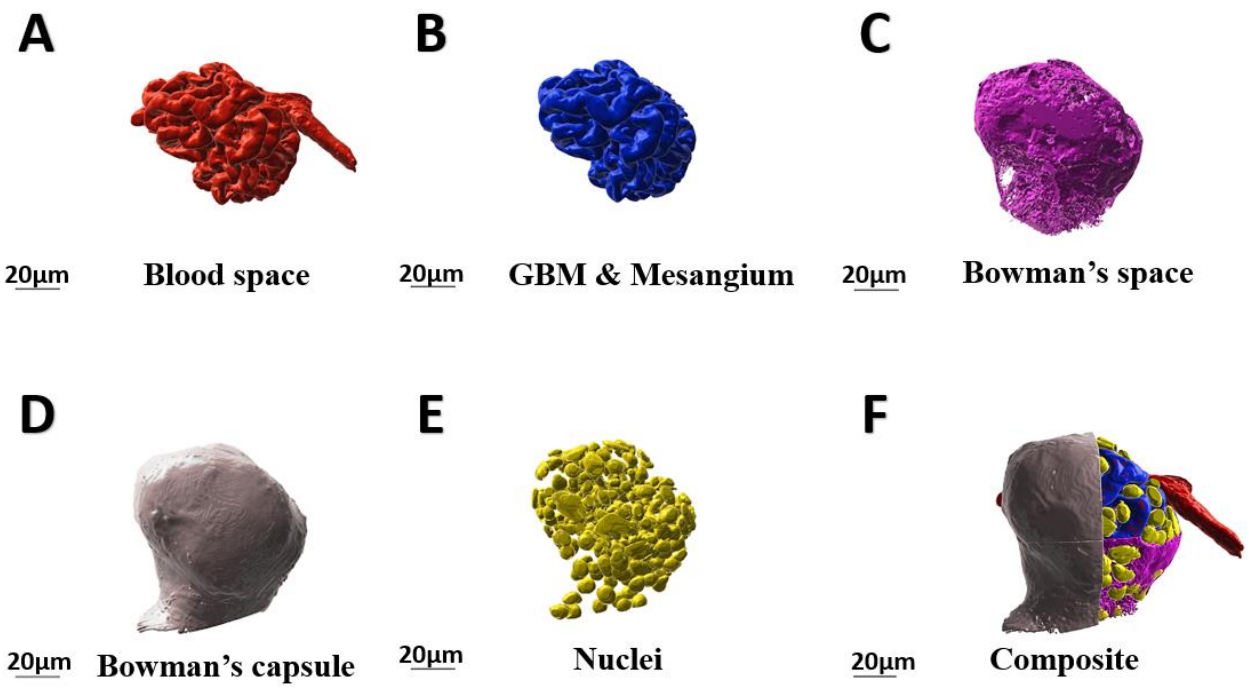

Figure 5. 3D reconstructed and rendered glomerulus structures: (A) Blood space, (B) GBM & mesangium, (C) Bowman's space, (D) Bowman's capsule, (E) Nuclei, (F) Composite volume of (A) - (E), Bowman's capsule and Bowman's space are shown with a partial cutaway view to reveal relative layering of different structures . Scale bars in (A) – (F) are shown in pre-expansion units.

Table 1. Statistics on different structural components of the glomerulus. All distances, areas, and volumes are in pre-expansion units.

V_{glom} (μm^3)	3.2 x 10^5
$Diameter_{Glom}$ (μm)	81.11
$V_{Blood\ Space}$ (μm^3)	5.8 x 10^4
$Diameter_{Afferent}$ (μm)	8.6
$Diameter_{Efferent}$ (μm)	6.9
$V_{Bowman's\ Space}$ (μm^3)	5.8 x 10^4
$V_{capsule}$ (μm^3)	3.3 x 10^4
$S_{capsule}$ (μm^2)	5.4 x 10^4
V_{GBM} (μm^3)	1.3 x 10^5
S_{GBM} (μm^2)	1.0 x 10^5
V_{Nuclei} (μm^3)	3.8 x 10^4
$Diameter_{PCT}$ (μm)	52.7

Table 2. Volume proportion of different structural components of the glomerulus.

	Volume fraction of the whole Glom
Blood Space	18%
GBM & Mesangium	40%
Bowman's Space	19%
Nuclei	12%
Bowman's Capsule	11%

We evaluated numerous parameters of the glomerulus, in part to validate the accuracy of the methodology (**Table 1**). The first and obvious choice was to obtain phenotypic parameters of the glomerulus as a whole unit. The glomerulus had a volume $3.2x10^5$ μm^3 (**Table 1**), which is in agreement with the previously reported value of $\sim 3\times10^5$ μm^3 for a mouse glomerulus [52], [53]. We defined the longest axis of the glomerulus as the diameter, which was determined to be 81.11 μm, which is also in accordance to previously reported average value of ~70 μm [20]. Each glomerular structure and their phenotypic information were then explored individually.

As the outermost protective "pouch" of the glomerulus, Bowman's capsule (**Figure 5D**)

has a surface area of 5.4 x 10^4 μm^2 and occupies 11% of the glomerular volume (**Table 2**). Three holes can be seen on the surface of Bowman's capsule (**Figure 6**). One hole is located at the vascular pole, where the afferent and efferent arterioles join the glomerulus **(Figure 6A**). Another hole at the urinary pole of the glomerulus opposite to the vascular pole (**Figure 6C**), where the glomerulus connects a proximal convoluted tubule with a diameter of 52.7 μm. A third hole was due to the insufficient imaging of the glomerulus towards the end of the stack (~10-20 slices missing), as shown in **Figure 6B**.

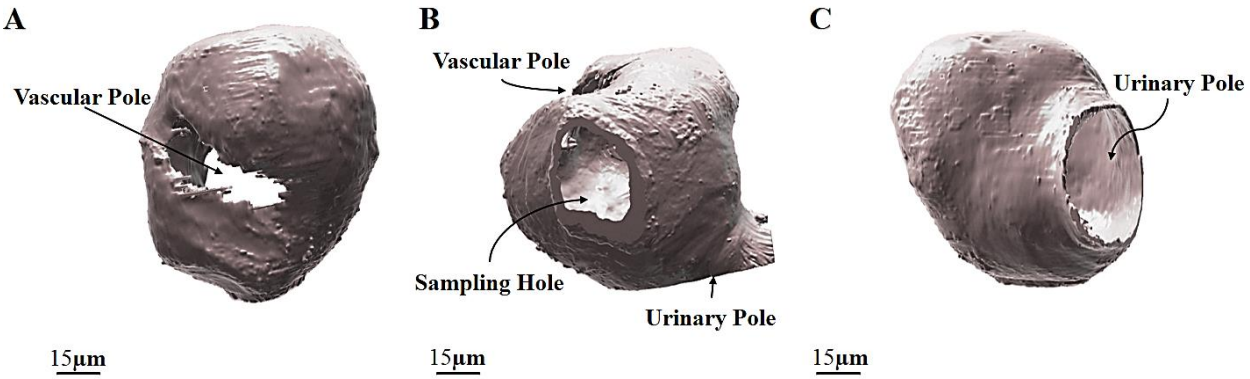

Figure. 6. Different views of Bowman's capsule showing three holes that are present. (**A**) The vascular hole. (B) The hole due to insufficient sampling. (C) The urinary hole. Scale bars are shown in pre-expansion units.

The volume of the blood space **(Figure 5A**) was 5.8 × 10^4 μm^3 (**Table 1**), taking up 18% of the glomerular volume (**Table 2**). The afferent arteriole entering the glomerulus (**Figure 7**, green arrows) was 8.6 μm wide, and the efferent arteriole (**Figure 7**, blue arrows) was 6.9 μm wide, which is close to previously reported values of around 8.9 μm and 7.4 μm respectively [54], [55]. These differences in the arteriole diameters and the fluid loss (about 20% of the input flow) during the filtration process together maintain a high hydrostatic pressure within the glomerulus

and the filtration process. In a study of the glomerular capillary network analysis by Terasaki et al., there seems to be a cleft-like gap where the capillaries are divided into an afferent half and an efferent half [20] with clear differences in size; a similar pattern was also seen in this glomerulus (**Figure 7**).

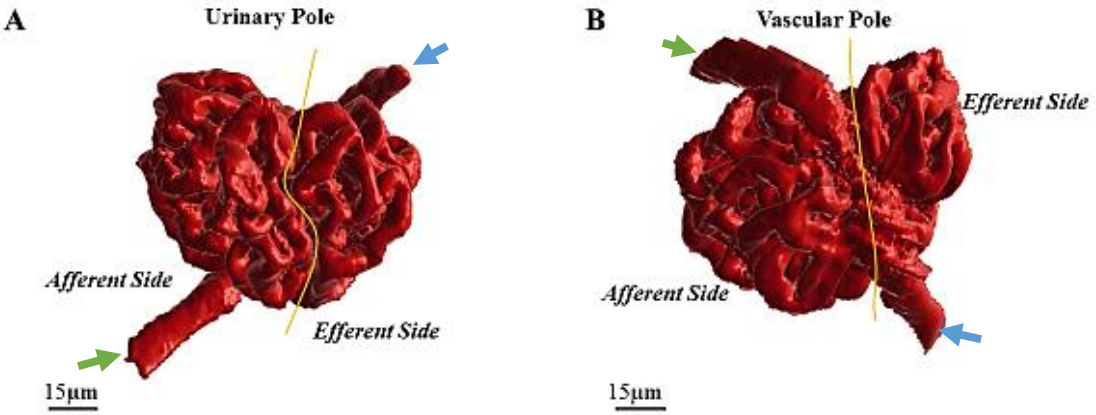

Figure 7. Views of the blood space from: (**A**) the urinary pole, (**B**) the vascular pole. The gap between the afferent and efferent arterioles is indicated by the yellow lines. The clear separation and the relative size difference between afferent and efferent arterioles are evident in both views. Green arrows = afferent arteriole. Blue arrow = efferent arteriole. Scale bars in A, B, and C are shown in pre-expansion units.

The GBM & mesangium was also reconstructed and rendered, shown in **Figure 5B**, which contained 40% of the glomerular volume (**Table 2**). The surface area was determined to be 3.8×10^4 μm^2 (**Table 1**). Due to the elasticity of the GBM, this area could change in response to the increase or decrease of capillary pressure [56]. In addition, many alterations such as thickening, thinning, and layering of GBM caused by different glomerular diseases can also affect the GBM surface area [57], [58]. Therefore, measuring the GBM surface area might provide valuable information on the differences among healthy, diseased, and aged glomeruli.

Cell type classification

In certain diseases, the disturbance to the glomerular structures is often found to be accompanied by changes to one or more cell types, for example, the proliferation of GECs and MCs in endocapillary proliferative glomerulonephritis, and proliferation of PECs in extracapillary proliferative glomerulonephritis [58]. Therefore, classifying different glomerular cell types within the GNSA and obtaining statistical observables would provide a valuable information on the connection between glomerular structures and glomerular cells and their roles in glomerular diseases. The ultimate goal is to find classifiers that could help us identify different glomerular cell types automatically based on size, shape, and relative position of their nuclei. To explore potential parameters that can be used for the classification task, glomerular cell nuclei were first reconstructed and rendered (**Figure 5E**). The five cell types were then manually identified within the glomerular space (**Figure 8**).

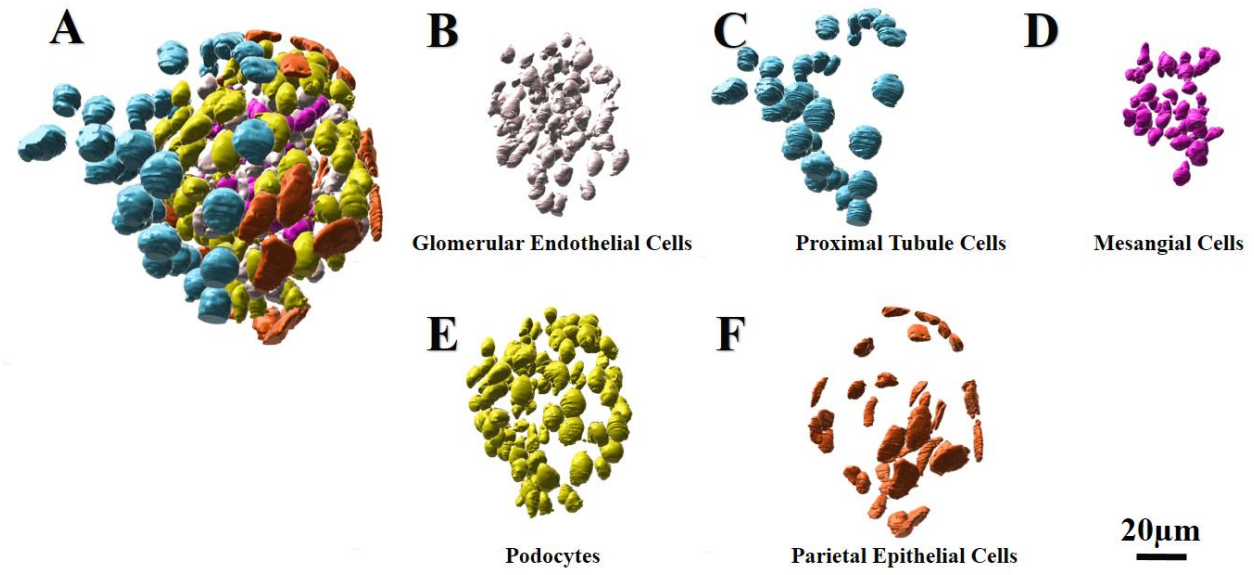

Figure 8. 3D rendered glomerular nuclei based on manual type classification result. (A) All nuclei

within the whole glomerulus. (B) Glomerular endothelial cells (GECs), (C) Proximal tubule cells (PCT), (D) Mesangial cells (MCs), (E) Podocytes, (F) Parietal epithelial cells (PECs). Scale bar is shown in pre-expansion unit.

Table 3. Measurements of the Numbers and Volumes for Nuclei of Glomerular Cell Types

Cell Type	Cell count	Count%
GECs	56	19%
MCs	72	25%
Podocytes	112	39%
PECs	39	13%
M/E uncertain	10	3%
Total	289	100%

*Proximal tubule cells are not included in this table. Ten cells were identified as either mesangial or endothelial cells (M/E uncertain) as they could not be confidently assigned to one group or the other.

Next, each individual cell types were studied separately. Forty PCT cells were identified (**Figure 8C**), which are the non-glomerular epithelial cells that make up the PCT basement membrane. As predicted, the PCT cells were the furthest away from the blood space (**Figure 9D**) as they reside at the urinary pole of the glomerulus **(Figure 10A**). Among all the cell types identified, the PCT cells were found to have the largest nuclear volume (**Figure 9A**).

Four primary types of glomerular cells - glomerular endothelial cells (GECs), mesangial cells (MCs), podocytes, and parietal endothelial cells (PECs) - were classified. There were a total of 289 glomerular cells with a combined nuclear volume of 3.8×10^4 μm^3 (**Table 1**), which made up 12% of the volume of the glomerulus (**Table 2**). The PECs are monolayers of squamous cells that have relatively flat cell bodies lining the outermost layer of the glomerulus. A total of 39 PECs

were identified (**Figure 8F**), composing 13% of the glomerular cells (**Table 3**). The nuclei of the reconstructed PECs nuclei appeared flat as compared to the others, as shown in **Figure 8F**. This observation is supported by the lowest sphericity value (**Figure 9B**), which measures how spherical an object is. As expected, the relatively flat PECs were the closest to the Bowman's capsule, with the shortest distance of 0 μm for all nuclei (**Figure 9C**) as they are at the glomerular periphery (**Figure 10B**). Changes in PECs are found to be associated with a variety of glomerular diseases. In crescentic glomerulonephritis, instead of forming a monolayer of cells, PECs proliferate a multilayered structure that releases extracellular matrix around them creating a cellular crescent [59], [60]. In another kidney disease example called focal segmental glomerulosclerosis, migration of PECs towards the glomerular tuft, and formation of cellular adhesion are evident [60], [61].

Looking a little deeper into the glomerulus, the podocytes are located outside and in proximity to the GBM & mesangium, which are an essential component of the glomerular filtration barrier. A total of 112 podocytes were identified. As shown in **Figure 10C**, the podocytes are sitting right on top of GBM surface, which is also supported by a short distance to blood space value in **Figure 9D**.

Finally, fifty-six GECs (**Figure 8B**) and 72 MCs (**Figure 8D**), which are located at the central core of the glomerulus, were classified, composing 19% and 25% of the total glomerular cells, respectively (**Table 3**). The GECs compose the fenestrated endothelium of the capillaries, whereas the MCs are positioned within the body of the mesangium. Due to the limitation of the staining and segmentation used at this stage in this project, the GBM and the mesangium were identified as a single entity. Unlike the relatively isolated environments of the PECs, PCT, and the podocytes, the classification of GECs and MCs was challenging, **Figure 10D** showed that the MCs

and GECs are both retained with the blood space we segmented. As a result of the complication, 10 nuclei were not able to be classified as either GECs or MCs with confidence and were instead classified as 'M/E uncertain'. As shown in **Figure 9A-D**, the parameters of the nuclei studied do not yet provide an easy way of successfully differentiating the GECs from the MCs. After careful observation through the 3D z-stack, MCs were enclosed by the GBM & mesangium signal, whereas the GECs were only partially covered at one side. Inspired by this correlation, we computationally dilated the GEC and MC nuclei volumes by 3 μm (in post-expansion unit) in all directions and measured the overlapping ratio of the dilated volume to the GBM & mesangium with a hypothesis that the MCs would have a higher overlap. This strategy allowed us to differentiate the MCs and GECs from one another much better than in the previous measurements, as shown in **Figure 9E**. It was obvious that the distribution of M/E uncertain cells are similar to the GECs, which might be an indication that these cells could be most likely classified as the GECs than MCs. However, further validation is needed.

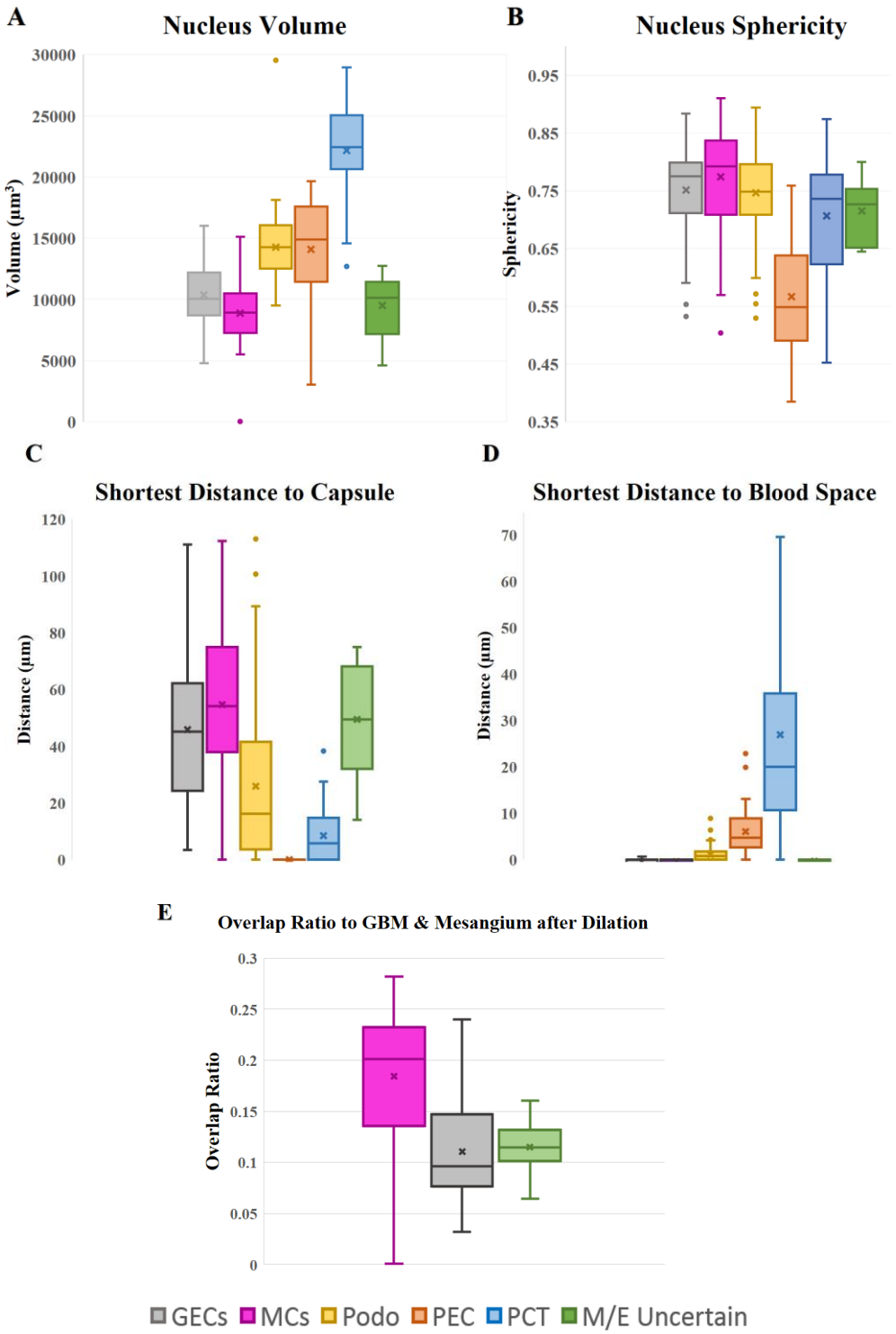

Figure 9. Boxplot of classified glomerular nuclei in different measurements: (A) Volume, (B) Shortest distance to Bowman's capsule, (C) Sphericity, (D) Shortest distance to blood space, (E) Overlap ratio to GBM & mesangium after dilation.

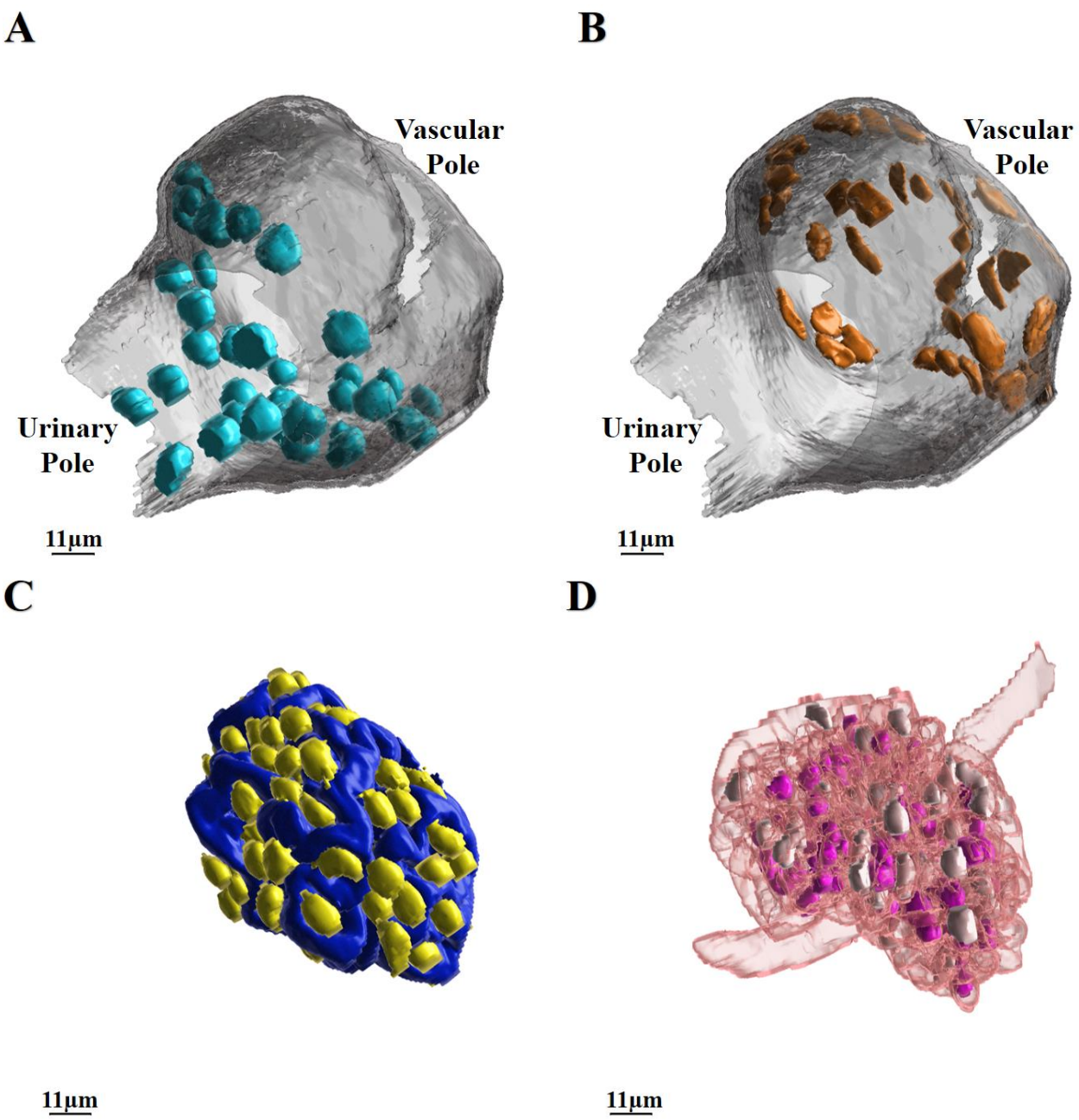

Figure 10. Relative spatial orientation between: (A) The PCT cell nuclei and the Bowman's capsule, (B) the PECs and the Bowman's capsule, (C) the podocytes and the GBM & mesangium, (D) the MCs/GECs and the blood space. Bowman's capsule in (A) and (B) and blood space in (D) are transparent processed for better visualization. Scale bars in (A)-(D) are in pre-expansion units.

Discussion and Future Directions:

I presented the 3D reconstruction and analysis work done for a glomerulus from a healthy female adult mouse here. This thesis indented to build the infrastructure for the GNSA. During the entire process of this thesis work, several limitations still apply.

The carbohydrate stain in the FLARE protocol labels the basement membrane of both the capillary loops and the mesangial matrix [50]. Due to the relative proximity and continuity of the carbohydrate signals from these two structures, distinguishing the GBM and the mesangium was challenging. Therefore, they were identified here as a single entity at this stage of GNSA development. The inability to distinguish the GBM and the mesangium had led to a chain of downstream effects in analyzing the first glomerulus. The glomerular blood space was obtained by filling the space enclosed by the segmented GBM & mesangium. This filling process inevitably misidentifies some of the mesangial space as the blood space, resulting in an inaccurate reconstruction. This further complicated the manual classification of the GECs and the MCs as the primary criteria used for classifying were the relative positioning of their nuclei to the GBM and the mesangium.

Several solutions will be explored in future work to solve this problem. First, co-immunostaining using either GECs specific markers (CD31, Endomucin etc.) or MCs specific markers (α8 integrin, PdgfrB etc.) along with three channeled FLARE staining. By co-staining either cell type in a fourth spectral channel, we could manually classify one cell type with confidence and safely assume the remainder to be classified as the other. Although this method clearly differentiates between the MCs and the GECs, the GBM vs. mesangium still would not be set apart. Another option is to label the blood vessels and the capillaries by cardiac perfusing fluorescently labeled molecules such as lipophilic carbocyanine dye Dil, [62], or Octadecyl

Rhodamine B [63]. The GBM vs. the mesangium and the GECs vs. the MCs will be readily distinguishable by labeling the glomerular capillaries. However, both co-immunostaining and vascular labeling methods are subject to fluorescent signal loss during the chemical staining and gelation procedures. The oxidizing agent used for carbohydrate labeling (sodium periodate) is, unfortunately, an efficient photo-bleaching agent for most fluorophores [50], and as a result, any fluorescent labeling present before carbohydrate oxidation will not be retained. An obvious solution would be performing additional staining after the carbohydrate oxidation. Nevertheless, as shown in **Figure 2A**, the relative order has to be followed for the following reasons. First, immunostaining after the expansion is significantly restricted by the hindrance of the dense polymer network to the large secondary antibody-dye complex. Second, it has been found that performing carbohydrate staining before gelation would cause obvious cracks within the tissue after expansion [50]. Therefore, this workflow has to be strictly followed if immunostain would be used in combination with the expanded flare sample.

Two routes will be taken in future work to circumvent this strict workflow and make staining of additional features possible. The first is to use a milder oxidizing agent that would not cause severe signal loss. I identified lead (IV) acetate from the literature as an effective agent for the oxidation of carbohydrates, similar to the periodate oxidation but with much milder conditions [64], [65]. We will first test the potential bleaching effect of lead (IV) acetate on our most commonly used fluorophores and then compare the staining pattern between the periodate and lead (IV) acetate to see if this will be a viable substitute. Furthermore, an alternative immunostaining modality will be examined to deliver fluorophores after chemical stain and gelation. This could be done by incubating the sample with the primary antibody as usual, followed by incubation with secondary-biotin conjugate that is not perturbed by periodate

oxidation [50], [51], and eventually delivering a dye-streptavidin conjugate after the gelation and the chemical stain. Penetration of the streptavidin-dye conjugate through the polymer network is less problematic due to the smaller size of streptavidin.

After potential improvements to the segmentation and analysis procedure, we want to expand the atlas to a collection of about 24 intact whole glomeruli in the GNSA in the future. Both healthy, aged, and diseased mice will be used to collect eight glomeruli from each group. The sex relevance of glomeruli morphology and diseases will also be explored by obtaining glomeruli from both male and female mice within each group. Although mice are a good model organism for studying various diseases due to having 99% similarity to the human genome, the fundamental difference between mice vs. humans would limit the ability to use a mouse model to study human diseases. The establishment of mouse GNSA would help us to have a better understanding of the glomeruli, eventually, leading us to follow-up studies on human glomeruli, which would be revolutionary for clinical studies of human kidney diseases.

Indeed, the reconstruction and analysis work in this thesis provided detailed annotated glomerular structures and supportive statistics on the first glomerulus. However, the manual and semi-automated method used in this work is very laborious, taking nearly 3 months of reconstruction for a single glomerulus and weeks of the classification of cell types. There is, therefore, a strong need to make this process automated. The goal in the near future will be to perform the reconstruction and analysis work for a couple of more glomeruli and use them as training datasets for a new collaboration with a computer science group at the University of Washington (Prof. Sheng Wang) to make this segmentation and cell-type classification fully automated via machine learning.

In conclusion, the first intact glomerulus was successfully reconstructed for the GNSA, and

the glomerular cell types were successfully classified. Both spatial and phenotypical statistics were obtained for the glomerular structures and cell types. In the later studies, additional statistical analyses such as capillary network analysis and membrane thickness distributions will be carried out. In this thesis work, I have established a pipeline that can determine the structures of interest and classify different glomerular cell types for an intact mouse glomerulus. This workflow will be further optimized and deployed for multiple glomeruli. The limitations and possible solutions of this work gave us reliable information and a clear direction for my future doctoral research, eventually leading to the establishment of the GNSA.

Material and Methods:

Reagents

Reagents for MAP protocol polymerization were purchased as follows: 40% (w/v) acrylamide (AA; Bio-Rad Laboratories, cat. no. 161-0140), 2% (w/v) bis-acrylamide (BA; Bio-Rad Laboratories, cat. no. 161-0142), Sodium acrylate (SA; Sigma-Aldrich, cat. no. 408220), VA-044 (Thermo Fisher Scientific, cat. no. NC0471397). Reagents for high temperature and detergent denaturation were purchased as follows: Sodium dodecyl sulfate (SDS; Sigma-Aldrich, cat. no. L3771), Tris base (Tris; Fisher Scientific, cat. no. BP152-500), Sodium chloride (NaCl; Fisher Scientific, cat. no. 271). Reagents for FLARE staining were purchased as follows: 10× phosphate-buffered saline, pH 7.4 (PBS; Fisher Bioreagents, cat. no. L-5400), Sodium azide (NaN_3; Fisher Scientific, cat. no. S227I), Sodium acetate, anhydrous (NaOAc; Fisher Scientific, cat. no. S209), 4-Morpholineethanesulfonic acid (MES; Sigma-Aldrich, cat. no. M8250), $NaIO_4$ (Sigma-Aldrich, cat. no. 311448), Sodium cyanoborohydride ($NaCNBH_3$; Sigma-Aldrich,

cat. no. 156159), ATTO-TEC GmbH, cat. no. AD565, ATTO 647N NHS ester (AT647N-NHS; Sigma-Aldrich, cat. no. 18373), ATTO 565 hydrazide (AT565-$NHNH_2$, Hoechst 33258 (Sigma-Aldrich, cat. no. B2883). Poly-L-lysine (P8920) was purchased from Sigma-Aldrich.

Mouse kidney tissue preparation

Anesthetized young female mice were cardiac perfused with 1× PBS/Azide and 4% PFA, each with 4 minutes and half. Both kidneys were harvested and renal capsule (the think film covering the kidney) were removed. Each kidney was fixed in 10 ml of 4% PFA for 1 hour. All procedures were approved and performed under the guidelines from the University of Washington Animal Use Training Session (AUTS) and the regulations from Institutional Animal Care and Use Committee (IACUC). After fixation, kidney was embedded in 4% (w/v) agarose in 1× PBS/Azide then sliced into 100um sections using vibratome. Kidney tissue sections were stored in 1× PBS/Azide at 4 ºC until further use.

Kidney tissue gelation, denaturation and expansion

100 µm thick kidney section was incubated in MAP monomer solution [20% (w/w) AA, 10% (w/v) SA, 0.05% (w/w) BA, and 4% (v/v) PFA] for 24 hours at 4 ºC. The section was then placed on a rectangular #1.5 coverslip and spread flat using a paint brush. Two stacked smaller pieces of #1.5 coverslips were placed on either end of the sample to act as spacers. A gelation solution was prepared by mixing 99 µl of pre-warmed MAP monomer solution with 1 µl of 10% (w/v) VA-44. A drop of the gelation solution (10-15 µl) was pipetted onto the tissue surface and covered with another piece of rectanguar #1.5 coverslip to create a gelation chamber (See **Figure 11** for a schematic of this setup). The gelation chamber is then placed into a glass chamber and

purged with sufficient nitrogen gas before closing the lid. Gelation was conducted for 2-2.5 hours at 45 ºC. After gelation, the gel is peeled off and placed in a scintillation vial containing denaturation solution [200 mM SDS, 200 mM NaCl, 50 mM Tris]. The denaturation was performed under 70 ºC for 18-24 hours and 95 ºC for another 18-24 hours. The gel was washed by PBST solution for three times, 30 minutes each, and one more wash with 1× PBS/Azide for another 30 minutes.

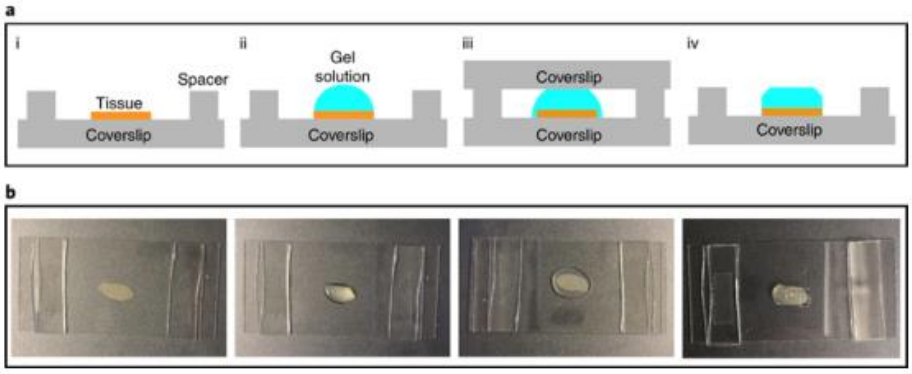

Figure 11. Schematic diagram with the MAP gelation chamber set up. Figure adapted from Lee et al., *Nat Protoc*., 2022.

FLARE staining protocol

Gelled tissue sample are stain in the order of carbohydrates, amines, and DNA. The sample was first oxidized with 2 ml of 20 mM NaIO4 in NaOAc/NaCl buffer for 1 hour at 37 ºC, protected from light with constant shaking, followed by three washes with NaOAc buffer for 10 minutes each. After oxidation, sample was then reacted in 1ml of 5 µg/ml AT565-Hydrazide in NaOAc for 3 hours at room temperature. The sample was finally reduced by addition 20 µl of 5 M $NaCNBH_4$ in NaOAc buffer for 30 minutes at room temperature. For staining amines, the sample is incubated with 2 ml of 5 µg/ml AT647N-NHS in MES buffer at pH 6 for 6 hours at room temperature. The

sample was then placed in large quantity of DI water for complete expansion overnight. Lastly, sample was stained with 1ml of 10 µg/ml Hoechst 33258 for 20 minutes at room temperature, followed by sufficient washes by DI water. All the above procedures were performed under protection of light with constant shaking.

Fluorescence image acquisition

The MAP-FLARE sample was fixed onto a poly-lysine coated cover glass to prevent drifting during imaging. Next, the sample was imaged using a scanning confocal microscope (Nikon A1R HD25 laser scanning confocal microscope, LSB B202A) at the University of Washington Biology Imaging Center. A 40× water immersion objective lens (Apochromat Lambda S LWD 40× water, NA 1.15, WD 0.59–0.61 mm) were used and a 0.5 µm z-step was taken for the 3-dimentional stack. A compromise on the resolution had to be taken considering the imaging time and the working distance of the objective. The 40× objective was chosen because it provides an adequate resolution (100 nm) for resolving key glomerular features while keeping imaging time in a reasonable range.

Glomerular structures identification and segmentation

Structure segmentation and identification were all done using ImageJ software using the following methods:

Full three-channel FLARE stained raw data stack were first split into carb, amine, and nucleus as separate stacks. The noise from carb stack was first cleaned up using *Process->Filters->Gaussian Blur* (A sigma of ~2 is sufficient for the first stack, however optimal number for value are dependent on the image acquired). The goal is to eliminate most of the “salt

& pepper" noise but keep most of the signal on the capsule as much as possible. Addition of a median filter might also help to remove the noise. The resulting stack was then binarized using *Process->Binary->Make Binary*. For the binary method, using either "Li", or "mean" gave the best result on keeping most of the capsule signal while minimizing other signals. Careful manual corrections were done along the capsule (shown in **Figure 4**, grey arrows) that appears to be discontinuous as a result of filtering and binarizing processes using the *Paintbrush Too*l (setting the pixel size to ~2). Incomplete closure of the capsule will cause more problems in the later part. After making the capsule all continues to circle, the *Paintbrush* tool was then used to erase all the other signal aside from the capsule **Figure 4**, gray arrows). The resulting file was saved as "Capsule_final".

The GBM & mesangium was segmented using exactly the same strategy as the capsule, with the only differences that instead of manual connecting fractured capsule signal along the grey arrows in **Figure 4**, the connection was done along the blue arrows in **Figure 4** instead. The resulting file was saved as "GBM & Mesangium_final".

The nuclei were segmented by first manually tracing all the cell nuclei periphery in the nuclei stack using the *Paintbrush* tool and then filled using *Process->Binary->Fill Holes* tool. The resulting file was saved as "Nuclei_final".

The blood space was identified by first filling the "GBM & Mesangium_final" stack using *Process->Binary->Fill Holes* tool. The "GBM & Mesangium_final", "Nuclei_final", and the amine channel stack were then subtracted from the filled GBM stack using *Process->Image Calculator* tool. The resulting file was saved as "Blood Space_final".

Lastly, the Bowman's space was identified by first inverting the carb channel and

thresholded. The “Blood Space_final”, “Nuclei_final”, and the amine channel stack were then subtracted from the inverted channel stack using *Process->Image Calculator* tool. The resulting file was saved as “Bowman’s Space_final”.

Glomerular structures reconstruction and analysis

The segmented five channel stack was imported to Imaris (RRID:SCR_007370). Each individual structure was reconstructed using the surface creation tool on Imaris. For specific instruction on the surface creation tool, see Imaris Reference Manual (https://imaris.oxinst.com/).

References

[1] "Your Kidneys & How They Work | NIDDK," *National Institute of Diabetes and Digestive and Kidney Diseases*. https://www.niddk.nih.gov/health-information/kidney-disease/kidneys-how-they-work (accessed May 08, 2022).

[2] S. Shankland, Y. Wang, A. Shaw, J. Vaughan, J. Pippin, and O. Wessely, "Podocyte Aging: Why and How Getting Old Matters," *JASN*, Sep. 2021, doi: 10.1681/ASN.2021-05-0614.

[3] L. Brown, "ClinicalKey," *J Med Libr Assoc*, vol. 101, no. 4, pp. 342–343, Oct. 2013, doi: 10.3163/1536-5050.101.4.023.

[4] R. J. Glassock and A. D. Rule, "The implications of anatomical and functional changes of the aging kidney: with an emphasis on the glomeruli," *Kidney International*, vol. 82, no. 3, pp. 270–277, Aug. 2012, doi: 10.1038/ki.2012.65.

[5] B. R. Hemmelgarn *et al.*, "Progression of kidney dysfunction in the community-dwelling elderly," *Kidney International*, vol. 69, no. 12, pp. 2155–2161, Jun. 2006, doi: 10.1038/sj.ki.5000270.

[6] Q.-L. Zhang and D. Rothenbacher, "Prevalence of chronic kidney disease in population-based studies: Systematic review," *BMC Public Health*, vol. 8, no. 1, p. 117, Apr. 2008, doi: 10.1186/1471-2458-8-117.

[7] S. Anderson and B. M. Brenner, "Effects of aging on the renal glomerulus," *The American Journal of Medicine*, vol. 80, no. 3, pp. 435–442, Mar. 1986, doi: 10.1016/0002-9343(86)90718-7.

[8] S. E. Quaggin and J. A. Kreidberg, "Development of the renal glomerulus: good neighbors and good fences," *Development*, vol. 135, no. 4, pp. 609–620, Feb. 2008, doi:

10.1242/dev.001081.

[9] J. Fu, K. Lee, P. Y. Chuang, Z. Liu, and J. C. He, “Glomerular endothelial cell injury and cross talk in diabetic kidney disease,” *American Journal of Physiology-Renal Physiology*, vol. 308, no. 4, pp. F287–F297, Feb. 2015, doi: 10.1152/ajprenal.00533.2014.

[10] J. Fu *et al.*, “Single-Cell RNA Profiling of Glomerular Cells Shows Dynamic Changes in Experimental Diabetic Kidney Disease,” *JASN*, vol. 30, no. 4, pp. 533–545, Apr. 2019, doi: 10.1681/ASN.2018090896.

[11] R. C. Wiggins, “The spectrum of podocytopathies: a unifying view of glomerular diseases,” *Kidney international*, vol. 71, no. 12, pp. 1205–1214, 2007.

[12] R. M. Mason and N. A. Wahab, “Extracellular Matrix Metabolism in Diabetic Nephropathy,” *JASN*, vol. 14, no. 5, pp. 1358–1373, May 2003, doi: 10.1097/01.ASN.0000065640.77499.D7.

[13] D. Schlöndorff and B. Banas, “The Mesangial Cell Revisited: No Cell Is an Island,” *JASN*, vol. 20, no. 6, pp. 1179–1187, Jun. 2009, doi: 10.1681/ASN.2008050549.

[14] J. H. Miner, “The Glomerular Basement Membrane,” *Exp Cell Res*, vol. 318, no. 9, pp. 973–978, May 2012, doi: 10.1016/j.yexcr.2012.02.031.

[15] M. R. Pollak, S. E. Quaggin, M. P. Hoenig, and L. D. Dworkin, “The Glomerulus: The Sphere of Influence,” *CJASN*, vol. 9, no. 8, pp. 1461–1469, Aug. 2014, doi: 10.2215/CJN.09400913.

[16] J. H. Suh and J. H. Miner, “The glomerular basement membrane as a barrier to albumin,” *Nat Rev Nephrol*, vol. 9, no. 8, Art. no. 8, Aug. 2013, doi: 10.1038/nrneph.2013.109.

[17] M. Simons and T. B. Huber, “It’s not all about nephrin,” *Kidney International*, vol. 73, no. 6, pp. 671–673, Mar. 2008, doi: 10.1038/sj.ki.5002798.

[18] M. C. Menon, P. Y. Chuang, and C. J. He, "The glomerular filtration barrier: components and crosstalk," *Int J Nephrol*, vol. 2012, p. 749010, 2012, doi: 10.1155/2012/749010.

[19] J. Reiser and M. M. Altintas, "Podocytes," *F1000Res*, vol. 5, p. F1000 Faculty Rev-114, Jan. 2016, doi: 10.12688/f1000research.7255.1.

[20] M. Terasaki, J. C. Brunson, and J. Sardi, "Analysis of the three dimensional structure of the kidney glomerulus capillary network," *Sci Rep*, vol. 10, no. 1, p. 20334, Dec. 2020, doi: 10.1038/s41598-020-77211-x.

[21] K. Ichimura *et al.*, "Three-dimensional architecture of podocytes revealed by block-face scanning electron microscopy," *Scientific Reports*, vol. 5, p. 8993, Mar. 2015, doi: 10.1038/srep08993.

[22] T. Burghardt *et al.*, "Advanced electron microscopic techniques provide a deeper insight into the peculiar features of podocytes," *American Journal of Physiology-Renal Physiology*, vol. 309, no. 12, pp. F1082–F1089, Dec. 2015, doi: 10.1152/ajprenal.00338.2015.

[23] D. Unnersjö-Jess, L. Scott, S. Z. Sevilla, J. Patrakka, H. Blom, and H. Brismar, "Confocal super-resolution imaging of the glomerular filtration barrier enabled by tissue expansion," *Kidney International*, vol. 93, no. 4, pp. 1008–1013, Apr. 2018, doi: 10.1016/j.kint.2017.09.019.

[24] D. Unnersjö-Jess, L. Scott, H. Blom, and H. Brismar, "Super-resolution stimulated emission depletion imaging of slit diaphragm proteins in optically cleared kidney tissue," *Kidney international*, vol. 89, no. 1, pp. 243–247, 2016.

[25] J. M. Pullman, J. Nylk, E. C. Campbell, F. J. Gunn-Moore, M. B. Prystowsky, and K. Dholakia, "Visualization of podocyte substructure with structured illumination microscopy (SIM): a new approach to nephrotic disease," *Biomed. Opt. Express, BOE*, vol. 7, no. 2, pp.

302–311, Feb. 2016, doi: 10.1364/BOE.7.000302.

[26] T. J. Chozinski *et al.*, "Volumetric, Nanoscale Optical Imaging of Mouse and Human Kidney via Expansion Microscopy," *Scientific Reports*, vol. 8, no. 1, Dec. 2018, doi: 10.1038/s41598-018-28694-2.

[27] M. J. Randles *et al.*, "Three-dimensional electron microscopy reveals the evolution of glomerular barrier injury," *Sci Rep*, vol. 6, no. 1, p. 35068, Oct. 2016, doi: 10.1038/srep35068.

[28] A. B. Fogo, "Minimal change disease and focal segmental glomerulosclerosis," *Nephrol. Dial. Transplant.*, vol. 16, no. suppl 6, pp. 74–76, Sep. 2001, doi: 10.1093/ndt/16.suppl_6.74.

[29] M. Vivarelli, L. Massella, B. Ruggiero, and F. Emma, "Minimal Change Disease," *CJASN*, vol. 12, no. 2, pp. 332–345, Feb. 2017, doi: 10.2215/CJN.05000516.

[30] "Minimal Change Disease," *UNC Kidney Center*. https://unckidneycenter.org/kidneyhealthlibrary/glomerular-disease/minimal-change-disease/ (accessed May 09, 2022).

[31] C. G. Galbraith and J. A. Galbraith, "Super-resolution microscopy at a glance," *Journal of Cell Science*, vol. 124, no. 10, pp. 1607–1611, May 2011, doi: 10.1242/jcs.080085.

[32] L. Schermelleh *et al.*, "Super-resolution microscopy demystified," *Nat Cell Biol*, vol. 21, no. 1, Art. no. 1, Jan. 2019, doi: 10.1038/s41556-018-0251-8.

[33] C. Coltharp and J. Xiao, "Superresolution microscopy for microbiology," *Cellular Microbiology*, vol. 14, no. 12, pp. 1808–1818, 2012, doi: 10.1111/cmi.12024.

[34] "Seeing beyond the limit: A guide to choosing the right super-resolution microscopy technique | Elsevier Enhanced Reader."

https://reader.elsevier.com/reader/sd/pii/S002192582100584 6?token=BD5038AFE0EF23DFAE46F929F81DB8158EFBBAADFA2E4BA81A47E7066B3A75A0A3B84B53957A4B87D736442CC278104B&originRegion=us-east-1&originCreation=20220508223651 (accessed May 08, 2022).

[35] M. L. Angelotti, G. Antonelli, C. Conte, and P. Romagnani, "Imaging the kidney: from light to super-resolution microscopy," *Nephrology Dialysis Transplantation*, vol. 36, no. 1, pp. 19–28, Jan. 2021, doi: 10.1093/ndt/gfz136.

[36] L. C. S. Wunderlich, F. Ströhl, S. Ströhl, O. Vanderpoorten, L. Mascheroni, and C. F. Kaminski, "Superresolving the kidney—a practical comparison of fluorescence nanoscopy of the glomerular filtration barrier," *Anal Bioanal Chem*, vol. 413, no. 4, pp. 1203–1214, Feb. 2021, doi: 10.1007/s00216-020-03084-8.

[37] E. L. Faulkner, S. G. Thomas, and R. K. Neely, "An introduction to the methodology of expansion microscopy," *The International Journal of Biochemistry & Cell Biology*, vol. 124, p. 105764, Jul. 2020, doi: 10.1016/j.biocel.2020.105764.

[38] A. T. Wassie, Y. Zhao, and E. S. Boyden, "Expansion microscopy: principles and uses in biological research," *Nat Methods*, vol. 16, no. 1, Art. no. 1, Jan. 2019, doi: 10.1038/s41592-018-0219-4.

[39] F. Chen, P. W. Tillberg, and E. S. Boyden, "Optical imaging. Expansion microscopy," *Science*, vol. 347, no. 6221, pp. 543–548, Jan. 2015, doi: 10.1126/science.1260088.

[40] T. J. Chozinski *et al.*, "Expansion microscopy with conventional antibodies and fluorescent proteins," *Nature Methods*, vol. 13, no. 6, pp. 485–488, Apr. 2016, doi: 10.1038/nmeth.3833.

[41] J. Woo *et al.*, "A Modified Magnified Analysis of Proteome (MAP) Method for Super-

Resolution Cell Imaging that Retains Fluorescence," *Sci Rep*, vol. 10, no. 1, Art. no. 1, Mar. 2020, doi: 10.1038/s41598-020-61156-2.

[42] K. S. Suvarna, C. Layton, and J. D. Bancroft, Eds., *Theory and practice of histological techniques*, 7. ed. Edinburgh: Elsevier Churchill Livingston, 2013.

[43] M. Titford, "The long history of hematoxylin," *Biotech Histochem*, vol. 80, no. 2, pp. 73–78, Apr. 2005, doi: 10.1080/10520290500138372.

[44] S. M. Bonsib, "Differential Diagnosis in Nephropathology: An Immunofluorescence-Driven Approach," *Advances in Anatomic Pathology*, vol. 9, no. 2, pp. 101–114, Mar. 2002.

[45] S. H. Nasr, M. E. Fidler, and S. M. Said, "Paraffin Immunofluorescence: A Valuable Ancillary Technique in Renal Pathology," *Kidney International Reports*, vol. 3, no. 6, pp. 1260–1266, Nov. 2018, doi: 10.1016/j.ekir.2018.07.008.

[46] P. W. Tillberg *et al.*, "Protein-retention expansion microscopy of cells and tissues labeled using standard fluorescent proteins and antibodies," *Nature Biotechnology*, vol. 34, no. 9, pp. 987–992, Jul. 2016, doi: 10.1038/nbt.3625.

[47] T. Ku *et al.*, "Multiplexed and scalable super-resolution imaging of three-dimensional protein localization in size-adjustable tissues," *Nature Biotechnology*, vol. 34, pp. 973–981, Jul. 2016, doi: 10.1038/nbt.3641.

[48] A. Francisco-Cruz, E. R. Parra, M. T. Tetzlaff, and I. I. Wistuba, "Multiplex Immunofluorescence Assays," *Methods Mol Biol*, vol. 2055, pp. 467–495, 2020, doi: 10.1007/978-1-4939-9773-2_22.

[49] K. Chen, R. Yan, L. Xiang, and K. Xu, "Excitation spectral microscopy for highly multiplexed fluorescence imaging and quantitative biosensing," *Light Sci Appl*, vol. 10, no.

1, p. 97, Dec. 2021, doi: 10.1038/s41377-021-00536-3.

[50] C. Mao *et al.*, "Feature-rich covalent stains for super-resolution and cleared tissue fluorescence microscopy," *Sci. Adv.*, vol. 6, no. 22, p. eaba4542, May 2020, doi: 10.1126/sciadv.aba4542.

[51] M. Y. Lee *et al.*, "Fluorescent labeling of abundant reactive entities (FLARE) for cleared-tissue and super-resolution microscopy," *Nat Protoc*, vol. 17, no. 3, pp. 819–846, Mar. 2022, doi: 10.1038/s41596-021-00667-2.

[52] E. J. Baldelomar, J. R. Charlton, K. A. deRonde, and K. M. Bennett, "In vivo measurements of kidney glomerular number and size in healthy and Os/+ mice using MRI," *American Journal of Physiology-Renal Physiology*, vol. 317, no. 4, pp. F865–F873, Oct. 2019, doi: 10.1152/ajprenal.00078.2019.

[53] B. D. Hann, E. J. Baldelomar, J. R. Charlton, and K. M. Bennett, "Measuring the intrarenal distribution of glomerular volumes from histological sections," *Am J Physiol Renal Physiol*, vol. 310, no. 11, pp. F1328-1336, Jun. 2016, doi: 10.1152/ajprenal.00382.2015.

[54] L. Zhao *et al.*, "High-salt diet induces outward remodelling of efferent arterioles in mice with reduced renal mass," *Acta Physiologica*, vol. 219, no. 3, pp. 654–661, 2017, doi: 10.1111/apha.12759.

[55] M. Kamiyama *et al.*, "Detailed Localization of Augmented Angiotensinogen mRNA and Protein in Proximal Tubule Segments of Diabetic Kidneys in Rats and Humans," *Int J Biol Sci*, vol. 10, no. 5, pp. 530–542, May 2014, doi: 10.7150/ijbs.8450.

[56] W. Kriz and K. V. Lemley, "Mechanical challenges to the glomerular filtration barrier: adaptations and pathway to sclerosis," *Pediatr Nephrol*, vol. 32, no. 3, pp. 405–417, Mar. 2017, doi: 10.1007/s00467-016-3358-9.

[57] R. W. Naylor, M. R. P. T. Morais, and R. Lennon, “Complexities of the glomerular basement membrane,” *Nat Rev Nephrol*, vol. 17, no. 2, Art. no. 2, Feb. 2021, doi: 10.1038/s41581-020-0329-y.

[58] “Patterns.” https://www.kidneypathology.com/English_version/Histologic_patterns.html (accessed May 07, 2022).

[59] L. Anguiano, R. Kain, and H.-J. Anders, “The glomerular crescent: triggers, evolution, resolution, and implications for therapy,” *Curr Opin Nephrol Hypertens*, vol. 29, no. 3, pp. 302–309, May 2020, doi: 10.1097/MNH.0000000000000596.

[60] S. J. Shankland, B. Smeets, J. W. Pippin, and M. J. Moeller, “The emergence of the glomerular parietal epithelial cell,” *Nat Rev Nephrol*, vol. 10, no. 3, Art. no. 3, Mar. 2014, doi: 10.1038/nrneph.2014.1.

[61] B. Smeets *et al.*, “Parietal epithelial cells participate in the formation of sclerotic lesions in focal segmental glomerulosclerosis,” *J Am Soc Nephrol*, vol. 22, no. 7, pp. 1262–1274, Jul. 2011, doi: 10.1681/ASN.2010090970.

[62] Y. Li, Y. Song, L. Zhao, G. Gaidosh, A. M. Laties, and R. Wen, “Direct labeling and visualization of blood vessels with lipophilic carbocyanine dye DiI,” *Nat Protoc*, vol. 3, no. 11, pp. 1703–1708, 2008, doi: 10.1038/nprot.2008.172.

[63] I. Khalin *et al.*, “Size-Selective Transfer of Lipid Nanoparticle-Based Drug Carriers Across the Blood Brain Barrier Via Vascular Occlusions Following Traumatic Brain Injury,” *Small*, vol. 18, no. 18, p. 2200302, 2022, doi: 10.1002/smll.202200302.

[64] G. I. Malinin, “Dimethyl sulfoxide-lead tetraacetate method for histochemical oxidation of polysaccharides.,” *J Histochem Cytochem.*, vol. 24, no. 2, pp. 443–447, Feb. 1976, doi: 10.1177/24.2.56394.

[65] V. Zitko and C. T. Bishop, “Oxidation of polysaccharides by lead tetraacetate in dimethyl sulfoxide,” *Can. J. Chem.*, vol. 44, no. 15, pp. 1748–1756, Aug. 1966, doi: 10.1139/v66-264.